# On the pathway of mineral deposition in larval zebrafish caudal fin bone

Anat Akiva [a], Guy Malkinson [b], Admir Masic [c], Michael Kerschnitzki [a], Mathieu Bennet [c], Peter Fratzl [c], Lia Addadi [a], Steve Weiner [a,*], Karina Yaniv [b]

[a] Department of Structural Biology, Weizmann Institute of Science, Rehovot, Israel
[b] Department of Biological Regulation, Weizmann Institute of Science, Rehovot, Israel
[c] Department of Biomaterials, Max Planck Institute of Colloids and Interfaces, Potsdam, Germany

## ARTICLE INFO

## ABSTRACT

A poorly understood aspect of bone biomineralization concerns the mechanisms whereby ions are sequestered from the environment, concentrated, and deposited in the extracellular matrix. In this study, we follow mineral deposition in the caudal fin of the zebrafish *larva* in vivo. Using fluorescence and cryo-SEM-microscopy, in combination with Raman and XRF spectroscopy, we detect the presence of intracellular mineral particles located between bones, and in close association with blood vessels. Calcium-rich particles are also located away from the mineralized bone, and these are also in close association with blood vessels. These observations challenge the view that mineral formation is restricted to osteoblast cells juxtaposed to bone, or to the extracellular matrix. Our results, derived from observations performed in living animals, contribute a new perspective to the comprehensive mechanism of bone formation in vertebrates, from the blood to the bone. More broadly, these findings may shed light on bone mineralization processes in other vertebrates, including humans.

## 1. Introduction

A long standing question in vertebrate biomineralization concerns when, where and in which form the first bone mineral is deposited along the pathway leading from the environment through the tissues to the final deposition site as carbonated apatite crystals. The modes of uptake of calcium, phosphate and carbonate ions necessary for vertebrate bone formation are diverse, reflecting the different habitats in which the organisms live. In teleost fish, water is presumably the major source of these ions [1]. The distribution of ions within the organism involves the circulatory system. Vertebrate blood and other body fluids are saturated with respect to carbonated hydroxyapatite, the mineral deposited in the skeleton [2]. Ectopic mineral deposition in soft tissues is prevented by the presence of proteins such as fetuin, matrix-Gla protein, osteopontin, and other macromolecules that inhibit crystal nucleation [3–6]. Calcium phosphate nanoclusters are thought to be present within the body fluids [7,8]. When precautions are taken to prevent unstable minerals from dissolving during sample preparation, mineral-bearing vesicles are observed inside cells close to forming bone [9], as well as in the extracellular matrix [10]. Granules composed of a calcium phosphate disordered phase are translocated from the cell to the extracellular space where bone forms [9,11,12]. In adult zebrafish

bone, the granules then infiltrate the collagen fibrils in the extracellular matrix, where they crystallize into carbonated hydroxyapatite [12]. In contrast to matrix vesicles [13–15], these granules are not membrane bound. In one case, elemental analysis of the intracellular granules from embryonic mice revealed a surprisingly low Ca/P ratio, raising the possibility that the mineral is a polyphosphate [11,16]. Raman spectroscopy of mineralizing mouse bone showed the presence of an octacalcium phosphate-like (OCP-like) precursor phase prior to the formation of the carbonated hydroxyapatite, and possibly amorphous calcium phosphate as well [17]. The crystalline phase of OCP differs from the apatite crystalline phase, by a water layer that is located between two layers of apatite [18]. The ACP → OCP → carbonated hydroxyapatite transformation reaction is known to occur in vitro at neutral pH conditions, as well as at physiological pH [19–22].

The zebrafish (*Danio rerio*) is an attractive model system for bone research due to its size, transparency, rapid development, and the availability of stable transgenic reporters, which label osteoblasts and blood vessels [23–28]. Several zebrafish studies focus on the bone formation process, and in particular on the different genes involved [26,29–32]. The bone–cell interface in the adult zebrafish caudal fin is well described. An artery is located at the center of two hemi-cylindrical bones, which together compose one ray [33–35]. A layer of osteoblast cells covers the hemi-cylindrical bone. Cells generally defined as fibroblasts are located in the gap between the artery and the osteoblast cells. The veins are located between different rays [34].

Here we investigate larval tail fin bone development in vivo and ex vivo. The larval tail is relatively thin and hence easy to analyze in

living *larvae* (Fig. 1a). Tail fin bone begins to develop at 17 days post-fertilization (dpf) and is fully formed by 30 dpf [36]. During this time, 18 fin bones are formed. The basic anatomy of the developing bone during the early stages is similar to the mature zebrafish ray anatomy described above [34,37]: two half cylinders with an artery (capillary) located in the middle of each bony-ray, and veins located between the bones (Fig. 1b–d). We used the fluorescent dye calcein, together with transgenic reporters, to monitor the calcium transport pathway and the distribution of calcium mineral-containing deposits in the tissue. Calcein is known to bind calcium [38,39] and to stain the newly formed bone surface [36] (Fig. 1a). We took advantage of the fact that up to 35 dpf, zebrafish *larvae* take up calcein directly from the water.

## 2. Materials and methods

### 2.1. Zebrafish husbandry

Adult and larval zebrafish were raised and maintained as previously described [40] and were handled according to the guidelines of the Weizmann Institute Animal Care and Use Committee. Embryos were generated by natural spawning and raised in egg water in a $28 \pm 0.5$ °C incubator. Three transgenic fish lines were used in this study: *Tg(fli1:EGFP)^{y1}* embryos expressing EGFP in endothelial/hematopoietic cells [23], were crossed to *nacre* mutants [41] to generate transparent animals enabling live imaging of juvenile stages (20–30 dpf); *Tg(fli1:DsRed)* [42] expressing DsRed in endothelial/hematopoietic cells; *Tg(osx:mCherry)* expressing mCherry under the regulation of the *osterix* promoter [43]. For imaging, *larvae* were treated with 0.003% phenyl-thiourea (PTU) to inhibit melanin pigment formation.

### 2.2. Angiography, calcein and DRAQ5 immersion

Microinjection was performed using a micromanipulator and a PV830 Pneumatic Pico Pump (World Precision Instruments, Sarasota, FL) as previously described [40]. The needle was inserted directly into the heart of an anesthetized larva. Calcein fluorescence was monitored right after injection. Calcein solution (Sigma Chemicals) 0.2% wt., was prepared by dissolving 2 g of calcein powder in 1 l water and adjusting the pH to 7 using NaOH and HCl [36]. The *larvae* were then immersed in this solution for different time periods (5–30 min), depending on their developmental stage. After rinsing the *larvae* in embryo water 3 times, they were imaged using a confocal fluorescence microscope. Note that the minimum time needed to start monitoring after injection was longer than the time lapse needed for appearance of the label in the bone, i.e. when the fish was first observed the bones were already fluorescently labeled.

DRAQ5 solution (BioStatus, United Kingdom) $0.25 \times 10^{-3}$ *v/v*, was prepared by diluting 1 μl of DRAQ5 solution in 4 ml water. The *larvae* were immersed in this solution for 5 h and rinsed in water before imaging.

### 2.3. Fluorescence imaging

An epifluorescence stereomicroscope (Leica M167FC) was used to image whole mount *larvae*. Pictures were taken using Leica Application Suite imaging software version 3.7 (Leica, Wetzlar, Germany). In-vivo imaging was performed on a Zeiss LSM 780 upright confocal microscope (Carl Zeiss, Jena, Germany) with a W-Plan Apochromat ×20 objective, NA 1.0. The green and red proteins and dyes were imaged sequentially as follows: green fluorescent proteins and calcein were excited at 488 nm and the emission was collected at 492/577 nm. Red fluorescent
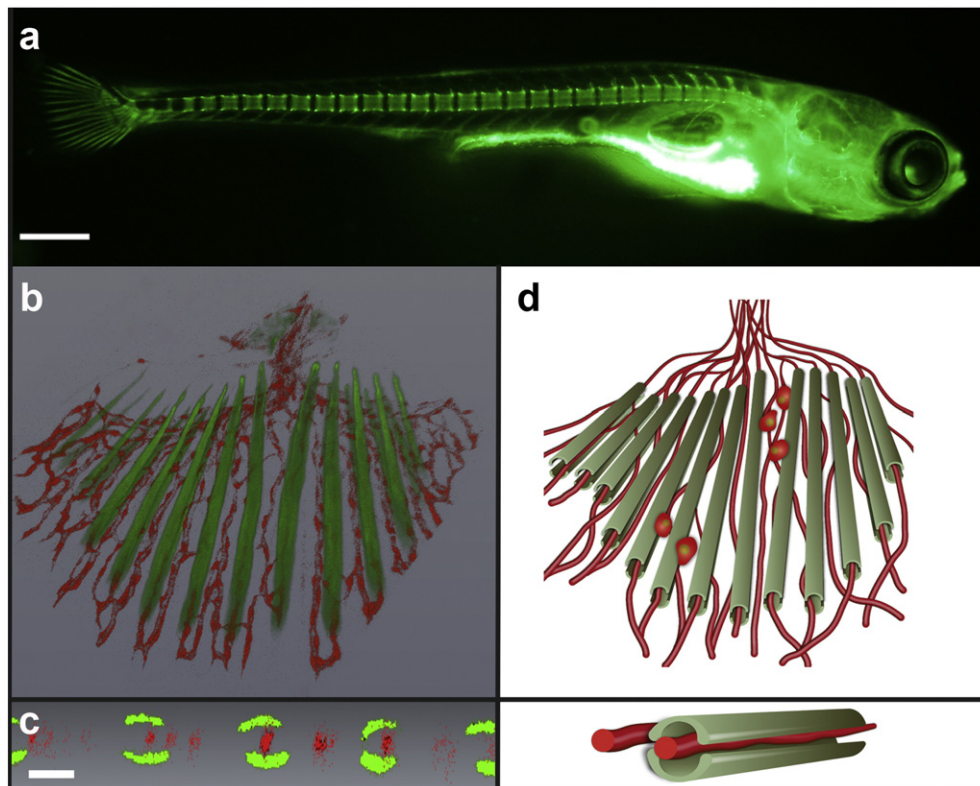


**Fig. 1.** The zebrafish bones: (a) 30 dpf zebrafish following 30 min immersion in calcein solution and suspension in water. The newly formed bones are stained with calcein. Scale bar: 1 mm. (b) Anatomical organization of the tail: confocal image of the zebrafish tail bones stained with calcein, and the endothelial cells marked with *fli1:DsRed*. Blood vessels first extend distally, and this is followed by bone formation. (c) Confocal image as in (b) of a transverse section of the tail: each fin bone is composed of two half cylinders, growing dorsally, and ventrally to the arteries. The veins are located between adjacent bone rays. Scale bar: 15 μm. (d) Schematic illustrations of the tail depicting: top (corresponding to b) the distribution of blood vessels, bones, and associated cells; bottom (corresponding to c) a single ray with the associated blood vessels.

proteins were excited at 561 nm, and the emission was collected at 568/629 nm. The DRAQ5 was excited at 633 nm, and the emission was collected at 644/735 nm. The *larvae* were anesthetized with tricaine–methanesulfonate (MS 222) (0.12%) and mounted in low-melting point-agarose (1.5%). Imaging was performed as previously described [44], using a custom-built chamber for perfusion of larvae with temperature-controlled physiological medium. Z-stacks were acquired at 1.5 μm increments, every 1 min. Images were processed off-line using ImageJ (NIH) and Avizo (FEI).

### 2.4. Embedded samples—TEM

Zebrafish larvae were fixed in 4% paraformaldehyde in cacodylate buffer and then dehydrated in ethanol carried out in 6 steps, each twice, for 10 min: 25%, 50%, 75%, 96%, and 100%. Larvae were then embedded in Epon (EMbed 812, EMS, USA), in 6 steps, each step for 8 h: 10%, 25%, 50%, 75%, 96%, and 100% resin, followed by 100% resin overnight and final embedding in a mold for 48 h at 60 °C. Ultrathin sections (70–90 nm) of the Epon embedded samples were cut by an ultramicrotome (UCT, Leica), double stained with Reynolds' lead citrate (10 min) and 2% uranyl acetate in ETOH (50 min). The samples were then viewed and photographed with an FEI Tecnai SPIRIT (FEI, Eidhoven, NL) transmission electron microscope operated at 120 kV and equipped with an EAGLE CCD camera.

### 2.5. Cryo-SEM

Tails were dissected from 25 to 30 dpf zebrafish, and were immersed immediately in 10% dextran (Fluka), sandwiched between two metal discs (3 mm diameter, 0.1-mm cavities with a flat cover above), and cryoimmobilized in a high-pressure freezing device (HPM10; Bal-Tec). The frozen samples were removed from the cavity, mounted on a holder under liquid nitrogen and transferred to a freeze fracture device (BAF 60; Bal-Tec) using a vacuum cryotransfer device (VCT 100; Bal-Tec). Samples were fractured at a temperature of −120 °C, etched for 10 min at −105 °C at a vacuum better than $5 \times 10^{-7}$ mbar. This preparation procedure was used to generate a transverse view of the bones (Fig. 2). Samples were observed in an Ultra 55 SEM ("Zeiss", Germany) by using a secondary electron in-lens detector and a backscattered electron in-lens detector (operating at 1 kV) in the frozen-hydrated state by use of a cryostage at a temperature of −120 °C.

### 2.6. Correlative fluorescence-Raman

The setup is based on the commercially available confocal Raman microscope (Alpha 300, WITec, Ulm, Germany) equipped with a helium neon (HeNe) laser (633 nm) laser excitation and piezoscanner (P-500, Physik Instrumente, Karlsruhe, Germany). The spectra were acquired with a thermoelectrically cooled CCD detector (DU401A-BV, Andor, UK) placed behind a grating (600 g mm$^{-1}$) spectrograph (UHTS 300; WITec, Ulm, Germany) with a spectral resolution of 3 cm$^{-1}$. The red laser beam (633 nm) was focused through a 10× (Nikon, NA = 0.2) and 60× water immersion (Nikon, NA = 1.0) microscope objectives. A pinhole size of 50 μm, was used. ScanCtrlSpectroscopyPlus software (version 1.38, Witec) was used for measurement and WITec Project Plus (version 2.10, Witec) for spectra processing. The implementation of the fluorescence modality relies on the substitutions of some of the original optics, integration of excitation light in addition to the white illumination light, and the addition of a module in the imaging arm, as described in [45].

### 2.7. Microbeam X-ray fluorescence (XRF)

In situ XRF measurements were obtained at the Nano Focus beamline ID 13 at the European Synchrotron Radiation Facility (ESRF), Grenoble, France. Samples were embedded in agarose and fixed on a kapton foil, which was clamped on a lead-tape window. The sample was mounted on a y–z scanning table and linear scans in areas of interest were performed with a step size of 1 μm using a monochromatic
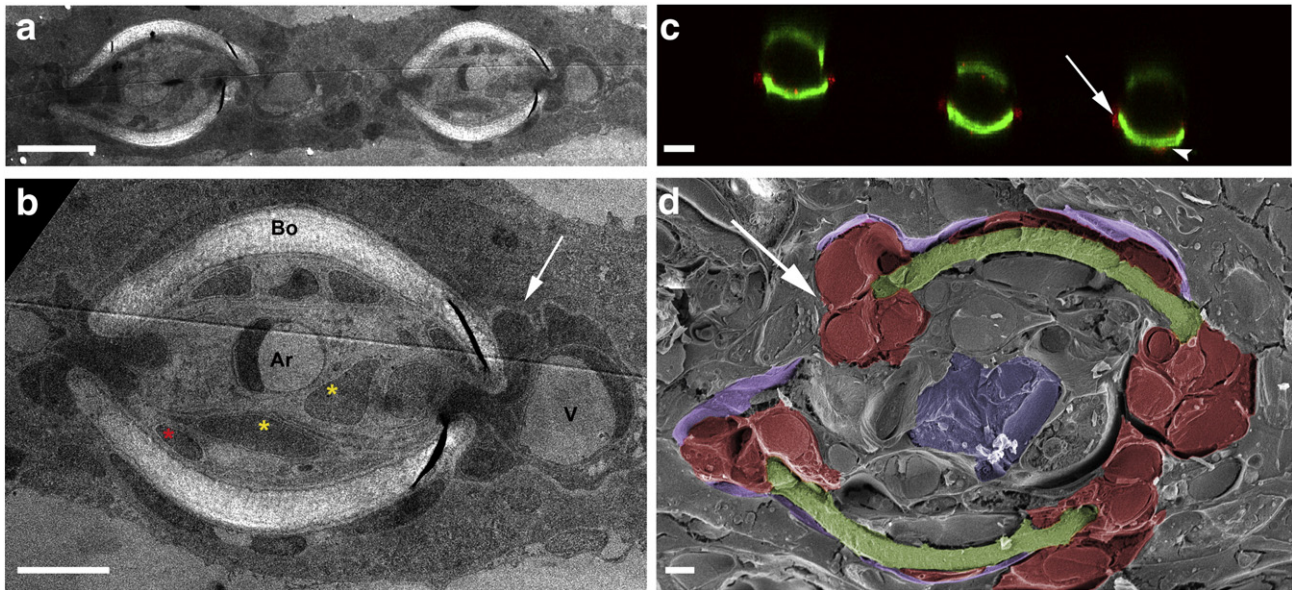


**Fig. 2.** Caudal fin transverse sections: (a). TEM image of a thin section of mineralized bones embedded in Epon following conventional methods, and post-stained with lead and uranyl acetate after slicing. (b). Higher magnification image of two bone hemi-cylinders forming one ray (Bo): the tissue between the two hemi-cylinders consists of two to three cell layers (yellow and red asterisks) that in adult zebrafish are identified as fibroblasts and bone-lining cells, respectively [34]. The artery (Ar) lined by a thin layer of endothelial cells is located between the two bones. The vein (V), located on the sides of each ray, is surrounded by cells that appear to extend to the edge of each bone hemi-cylinder. (c). Three bone hemi-cylinders (green, calcein) of a transgenic zebrafish expressing red fluorescence in *osterix*-positive cells *Tg(osx:mCherry)*. The *osterix* positive cells are located mainly at the edges of each hemi-cylinder (arrow), but also line the bone (arrowhead). The image was taken from a z stack on a living zebrafish larva. (d). Cryo-SEM image with pseudo coloring of one bony ray (green) and the associated tissue: the bones are covered by a membrane (light purple), and are surrounded by a cell layer, which comprises cells of different morphologies. A blood vessel is located between the two bones (light blue). The cells which are colored in red are located in positions equivalent to the osterix positive cells in c. Scale bars: a 10 μm, b, c, d 2 μm.

X-ray beam with an energy of 14 keV. Fluorescence spectra were collected with a fluorescence detector in transmission geometry at an angle of about 45°. The K-shell fluorescence yield of calcium, normalized to the primary beam intensity, was used to qualitatively map the position of bone segments within the tissue.

### 2.8. Analyzing SEM and fluorescence data

Fluorescence images were processed using ImageJ (National Institutes of Health, Bethesda, MD), and Avizo (VSG). Adobe Photoshop (San Jose, CA) software was used for adjusting brightness and contrast levels and for pseudo-coloring.

## 3. Results

### 3.1. Description of the tissue

We begin by describing the anatomy of the developing caudal fin at high resolution using TEM and cryo-SEM, followed by confocal imaging of *Tg(osx:mCherry)*[43] zebrafish, which carry a fluorescent reporter in (pre)osteoblasts. The TEM images of an embedded sample show similar features to those reported in the literature for larval zebrafish tail [35], including the bone hemi-cylinders, the blood vessels and the associated tissues (Fig. 2a,b). The bones are easily detected by their unique hemi-cylindrical shape and mineralized bone texture. The artery is located between the two rays. The vein, which is larger in diameter than the artery, is located between adjacent rays. Two to three layers of cells separate the artery from the bone. Some of the cells, located in close proximity to the vein, extend to the edges of the hemi-cylinders (Fig. 2a,b arrows). Confocal imaging of *Tg(osx:mCherry) larvae*, which are labeled with mCherry (red) in (pre)osteoblasts (osterix), and calcein (green) in bone, revealed the location of the (pre)osteoblast cells relative to the bones (Fig. 2c). Surprisingly, the *osterix*-positive cells were clearly detected at the edges of each hemi-cylinder (Fig. 2c, arrow), but did not completely surround the bone surface (Fig. 2c, arrowhead).

A comparison between the fluorescence images of the *osterix*-positive cells and the TEM images, suggests that the cells observed at the edges of the hemi-cylinder bone cross section are (pre)osteoblasts. The cell morphology in the TEM, however, does not enable clear identification of the (pre)osteoblast cells. To obtain a better morphological characterization of these cells, we carried out cryo-SEM on transverse sections of the rays (Fig. 2d). The sample preparation process in cryo-SEM involves only rapid high-pressure freezing, allowing preservation of the tissue under conditions that resemble its native state. In contrast, sample preparation for conventional TEM requires more invasive pre-treatment such as fixation, dehydration, staining and embedding, which can affect the shape, texture and composition of the biological specimen. The cryo-SEM images correlate well with the TEM images as far as the bone, artery and cell locations are concerned. The cell morphologies and the general dimensions are, however, substantially different. These differences are attributed to the dehydration process in the TEM, whereby pronounced unidirectional collapse of the soft tissue between the rigid bone hemi-cylinders occurs. As a consequence, the bone hemi-cylinders appear much closer to each other in the TEM, and the cells at the edges are deformed. Different cell morphologies are detected in cryo-SEM (Fig. 2d): the cells that are located at the edges have rounded shapes (arrows). The rounded cell location is similar to that of the *osterix* transcription factor expressing cells in the fluorescence images. These cells are pre-osteoblasts and/or osteoblasts. Some, but not all of the longer and thinner cells that line the bones, and are *osterix*-positive, are also assumed to be osteoblasts. In addition, cryo-SEM micrographs show a membrane surrounding the whole bone complex.

### 3.2. In vivo calcein labeling experiments

Live zebrafish *larvae* were immersed in water containing the fluorescent marker calcein (0.2% wt.) [36], and were imaged using confocal microscopy. Two zebrafish transgenic reporters highlighting endothelial cells were used in these experiments: *Tg(f1i1:DsRed)* (red fluorescence) and *Tg(fli1:EGFP)* (green fluorescence). Uptake of calcein from the water into the larval bones was found to take place within ~3 min for 6 dpf *larvae*, and 30 min for 30 dpf *larvae* (Fig. 1a) [36]. Immediately after immersion, the fish gut is strongly stained by the calcein dye, suggesting that the calcein passes directly through the digestive system and not by diffusion through the fish epidermal layer. Note that dead larvae do not take up calcein. When calcein (0.2% wt.) was injected directly into the blood circulation using microangiography (~25 dpf), the bones were labeled with calcein within a few minutes following the injection. Because of the quasi-instantaneous appearance of the label in the bone, it is conceivable that calcein is transported to the bone surface in part directly from the blood vessels. At later stages (~35 dpf), when the initial formation of the caudal fin is complete, bone labeling by immersion of the fish in calcein solution takes several hours, indicating that a different mechanism for calcein transport or interaction might be active.

### 3.3. Calcium deposits in close association with blood vessels

At ~25 dpf, in addition to the calcein stained bones, we also observed concentrated calcein stained particles, and particle aggregates (Fig. 3a (arrow and arrowhead)). Some of these aggregates were detected close to the bone rays (Fig. 3a arrowhead, c, d), but many were located at some distance from the bone rays and close to the blood vessels (Fig. 3a, arrow). A strong calcein signal was observed from some particles close to the bone within the cytoplasm of *fli1*-positive cells (Fig. 3c, Supplementary Movie 1, and Supplementary Fig. 1). To confirm that the *fli1*$^+$ signal is indeed from cells which carry mineral particles, the live nuclei stain DRAQ5 was used. We imaged *Tg(fli1:EGFP) larvae*, labeled with calcein (mineral particles), and DRAQ5 (far red emission). Ideally we could have demonstrated this using calcein blue to optimize the contrast between the *fli1*$^+$ EGFP green label and the calcein label. Unfortunately the signal from calcein blue is weak, and thus difficult to identify. Despite the problem of using two green labels, the intensity differences still enable us to visualize mineral particles located adjacent to the cell nuclei in *fli1*-positive cells. We therefore confirm that the calcein dense particles are intracellular (Fig. 3d, supplementary Fig. 2).

Intracellular vesicular bodies of sizes <1 μm, which closely resemble mineral particles, were observed by cryo-SEM in bone-lining cells (Fig. 3e). Small calcein fluorescent particles (~1 μm) were also distributed all over the tail (Fig. 3a). In some cases, the small particles formed larger aggregates, (~7 μm) (Fig. 3a, arrow), which were more abundant in the distal part of the tail, where the bone was not yet mineralized. In all cases, the calcein stained aggregates were located very close to a blood vessel (stained red in the figures). To confirm that the calcein labeled aggregates are indeed tagging calcium mineral particles, we used X-ray fluorescence (XRF) (Fig. 3b) with 1 μm beam resolution to localize and map the calcium distribution in the entire tissue of a zebrafish tail. We observed small particles (~1 μm) and larger particle aggregates of ~7 μm that contain calcium (Fig. 3b inset) at locations where we had previously observed calcein binding aggregates. Maps of phosphorus and sulfur obtained in the same areas show particles that have co-localization of calcium, phosphate and sulfur (supplementary Fig. 3). We therefore conclude that the calcein fluorescence is mapping deposits of a calcium phosphate mineral in the tail fin tissue. The large mineral-containing aggregates were detected mainly in the regions where the bone had not yet formed, or was just forming. It is not clear whether the large aggregates are in vesicles within or outside cells or whether these aggregates are associated with the collagen matrix of the soon-to-be mineralized bone.
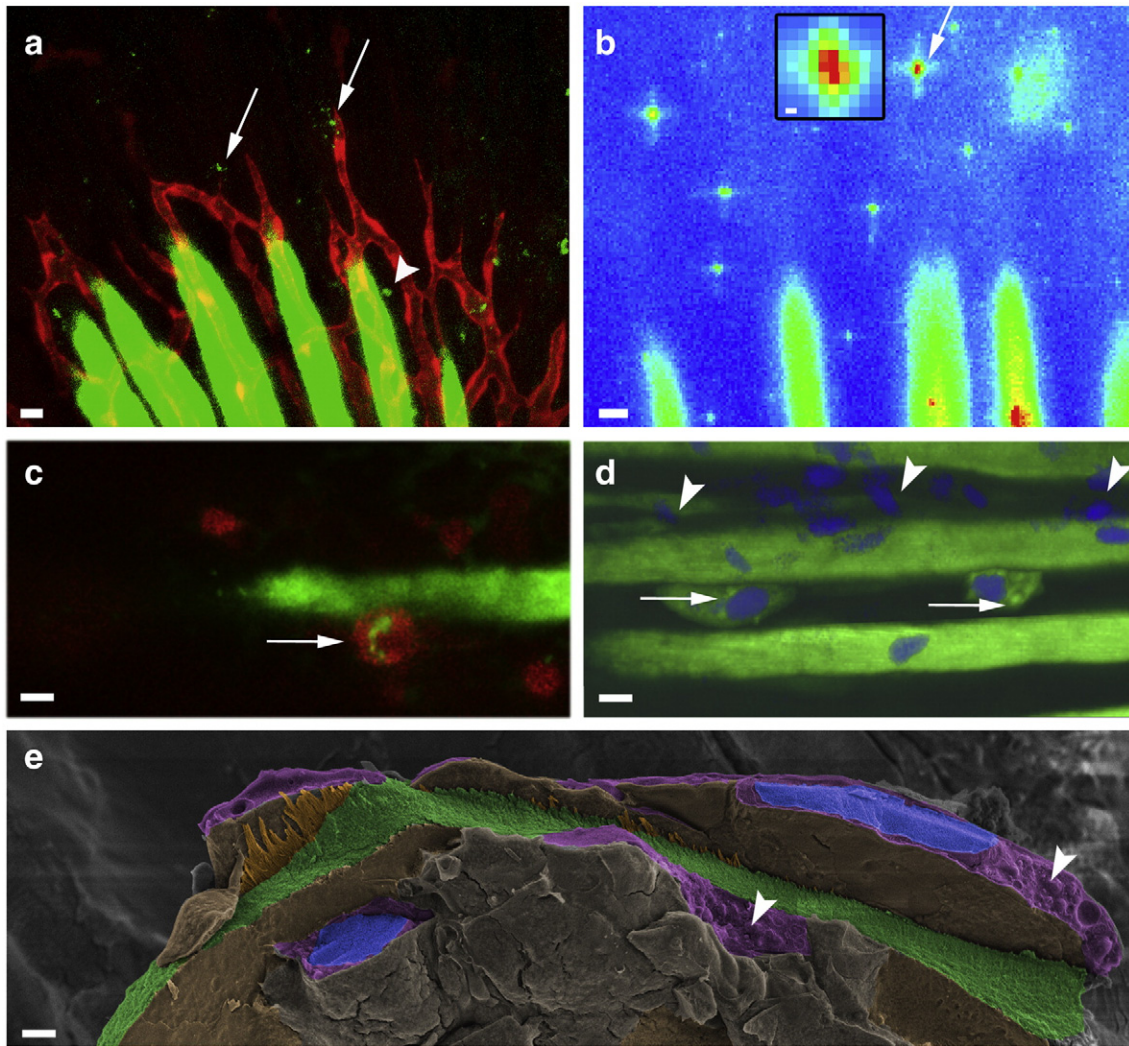
**Fig. 3.** Calcium particle distribution in the zebrafish tail. (a) In vivo confocal imaging of a *Tg(fli1:DsRed)* zebrafish *larva* tail. The mineral (bone and mineral deposits) is stained with the green fluorescent marker calcein. Endothelial cells exhibit red fluorescence. Several particles are detected next to the blood vessel (arrow) in addition to particles of 1 μm, which are spread throughout the tail (arrowheads). (b) Calcium XRF map of a similar region showing the distribution of calcium in locations equivalent to those imaged with confocal microscopy in Fig. 3a (arrow). Inset: A calcium-containing deposit located in the non-mineralized collagen region in the distal part of the tail imaged by calcium XRF mapping. The sphere has a diameter of ~7 μm. Color scale for the XRF maps: Blue: no calcium, green: intermediate calcium concentration, red: high calcium concentration (c, d) Co-localization of calcein deposits and cells: (c) Calcein stained particles are detected within a *fli1*-positive cell (arrow), in *Tg(fli1:DsRed)* larvae. (see also Supplementary Movie 1). (d) *Tg(fli1:EGFP)*, calcein and DRAQ5 staining of the cell nuclei (pseudo-colored blue). Micrometer-size particles with high calcein content are detected within the cells (arrows). Note that not all DRAQ5 positive cells carry calcein within their cytoplasm (arrowheads) (see supplementary Fig. 2 for lower magnification of the imaged region) *Tg(fli1:EGFP)* was used here because the DRAQ5 and DsRed marker excitations overlap. (e) Pseudo-colored cryo-SEM micrograph of a bone cylinder (green) with the surrounding soft tissue. Blue: cell nuclei; orange: non-mineralized collagen; pink: bone-lining cell cytoplasm, containing vesicular bodies. Scale bars (a–d): 10 μm. (d inset, e): 1 μm.

### 3.4. Calcium deposits between bone hemi-cylinders

Small particles with high calcein concentrations, presumably labeling mineral deposits, were observed between the artery and the inner bone surface (Fig. 4a,b. Supplementary Movie 1). Cryo-SEM images of the hemi-cylindrical bones and the associated soft tissue occasionally show clusters of vesicles (Fig. 4c,d) in locations equivalent to those of the fluorescent particles. The vesicles in both images (Fig. 4a,c) are in the sub-micrometer size range, and contain mineral (see next section).

### 3.5. Identification of the mineral phase in the aggregates

In order to obtain information on the mineral phase in vivo, we used Raman microspectroscopy correlated with fluorescence imaging [45]. In this correlative approach, the fluorescence and Raman scattered light share the same optical path and can be detected simultaneously. We first used fluorescence imaging to localize the region of interest (ROI), and then acquired the Raman spectrum from the very same ROI. The spatial resolution of the Raman confocal microscope is limited by the depth of the acquisition of the scattered light in the tissue. Under the conditions used (see Methods), the lateral and axial resolutions are ~1 μm and 3 μm respectively.

Anesthetized *Tg(fli1:EGFP)*[y1] nacre fish without pigments [41] were mounted on a microscope slide after immersion in calcein solution for 30 min and rinsed in water. The bones and blood vessels were identified by means of fluorescence contrast (Fig. 5a). The mineral aggregate distribution is not homogeneous throughout the tail. In order to locate regions of high mineral concentrations between two bone hemi-cylinders, we scanned the bones in the XY plane and the ZY plane (Fig. 5b). Following this procedure, mineral was located between the two hemi-cylinders, at a distance that was at least twofold larger than the resolution, thus ensuring that the detected signal did not originate from the bone itself. The bone spectrum (Fig. 5c, black) shows
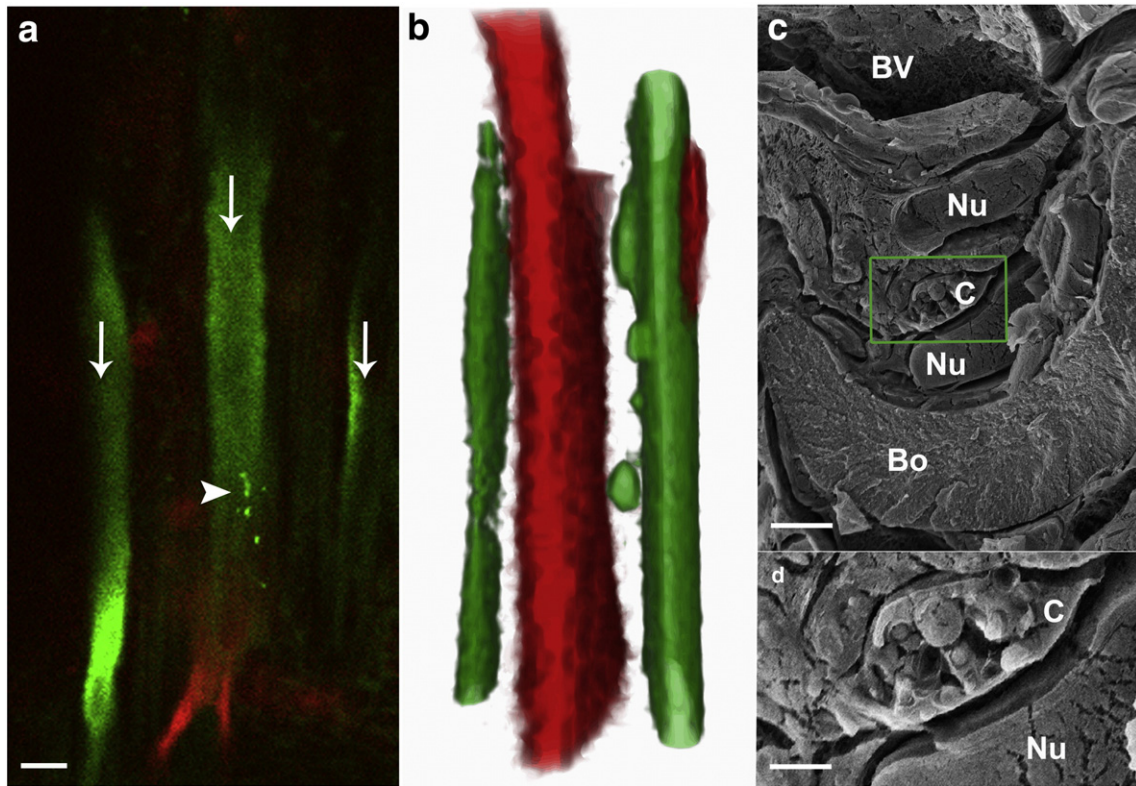
**Fig. 4.** Particles in the intra-ray region: (a) Micrometer-size particles (arrowhead) are detected in the inner part of the cylindrical bone (arrow). (Calcein (green) labels mineralized bone and particles. Red: fli1 marker labels endothelial cells). (See also Supplementary Movie 1). Scale bar: 10 µm. (b) 3D reconstruction of the same image as in panel A showing that mineral particles (green) are located between the artery (red) and the bones (green), thickening the bone from the inner side of the hemi-cylindrical bone. (c) InLens secondary electron image using cryo-SEM in transverse section on the inner side of one hemi-cylindrical bone. Bo: bone; Nu: nucleus; C: cluster; BV: blood vessel. Scale bar: 2 µm. (d) Higher magnification of the vesicles delineated by a rectangle in panel c. scale bar: 1 µm.

characteristic features of newly deposited bone, namely the mineral $PO_4^{3-}$ vibration (labeled $\nu_1$ $PO_4$ at 960 cm$^{-1}$), and the characteristic $HPO_4^{2-}$ spectral signatures that are characteristic of freshly deposited bone mineral [46]. In contrast to this newly deposited bone, the mineral aggregates in the tissue generated spectra with phosphate $\nu_1$ $PO_4$ peaks of lower intensity (Fig. 5, blue and red spectra; supplementary Fig. 4 for the non-mineralized soft tissue reference), and spectral features (Fig. 5, inset) characterized by: (i) a shift of the main $\nu_1$ $PO_4$ peak from 960 cm$^{-1}$ to 955–958 cm$^{-1}$ (the range observed for several calcium phosphate deposits that were found next to bones); (ii) presence of a peak at 967 cm$^{-1}$; and (iii) a broad peak centered at ~945 cm$^{-1}$. The main $\nu_1$ $PO_4$ peak of the mineral deposits centered at 955–958 cm$^{-1}$ is neither a typical Raman amorphous calcium phosphate (ACP) peak, nor a typical peak of carbonated apatite. ACP with a Ca/P ratio of 1.4 is known to absorb around 950 cm$^{-1}$ [46,47], and carbonated apatite at 960 cm$^{-1}$ [46]. The $\nu_1$ $PO_4$ peak at 967 cm$^{-1}$, accompanied by the 955 cm$^{-1}$ peak, has been attributed to an octacalcium phosphate like (OCP-like) phase [46]. A similar set of peaks was observed by Crane et al. [17] using Raman spectroscopy in the coronal suture of a mice tissue culture, and was assigned to an OCP-like phase (955 cm$^{-1}$ and 970 cm$^{-1}$) and ACP (945 cm$^{-1}$). Reference spectra of ACP, OCP and carbonated HA are shown in supplementary Fig. 5 for comparison.

Interestingly, in both newly deposited bone and mineral aggregates, a series of peaks in the range of 700 to 800 cm$^{-1}$ were observed. These peaks can be assigned to the ring breathing modes of pyrimidine bases (C, T, and U) of DNA and RNA related molecules, as well as the phospho-diester bridges [48–52]. Additionally, a peak located at 1090 cm$^{-1}$, that can be assigned to the phosphodioxy symmetric stretching (e. g. nucleic acids backbone), was observed in the mineral deposits [52] (supplementary Fig. 4).

## 4. Discussion

Here we show that intra-cellular and extra-cellular micrometer-sized mineral deposits are formed in tail fin tissues at some distance from the forming bones, and in many cases in proximity to the forming vascular system. Mineral deposits close to the forming fin bones were also observed, as was previously reported in adult zebrafish [12]. Our results suggest that during bone formation, the mineralization pathway in zebrafish involves other cells and processes, over and above the cells adjacent to the forming bone, which deposit the initial disordered mineral phase and transport it into the extracellular bone matrix. An analogous observation was made in the developing sea urchin *larvae*, where mineral deposits were observed in cells not known to be directly involved in spicule formation [53].

The intimate association of the vascular system with forming bones [54,55] is confirmed by showing that in the forming zebrafish tail, both ingested calcein, and calcein injected directly into the blood stream, reach the tail fin tissues and stain the bones within minutes. Blood circulation is clearly intimately involved in calcium transport. This in turn raises the question of whether or not calcium phosphate aggregates form in the blood itself [7,8].

The time scale for bone labeling by calcein changes dramatically when the larvae reach the age of ~35 dpf. At this stage, the initial formation of the caudal fin is complete. Prior to this stage, only a few minutes are required for the bone to be homogenously labeled. After this stage (>35 dpf), bone labeling by immersion of the fish in calcein solution takes several hours. This may indicate that different mechanisms for calcein transport are active before and after 35 dpf. Assuming that calcium and calcein share the same pathway, we infer that during the early stage (<35 dpf) when initial bone mineralization occurs, the
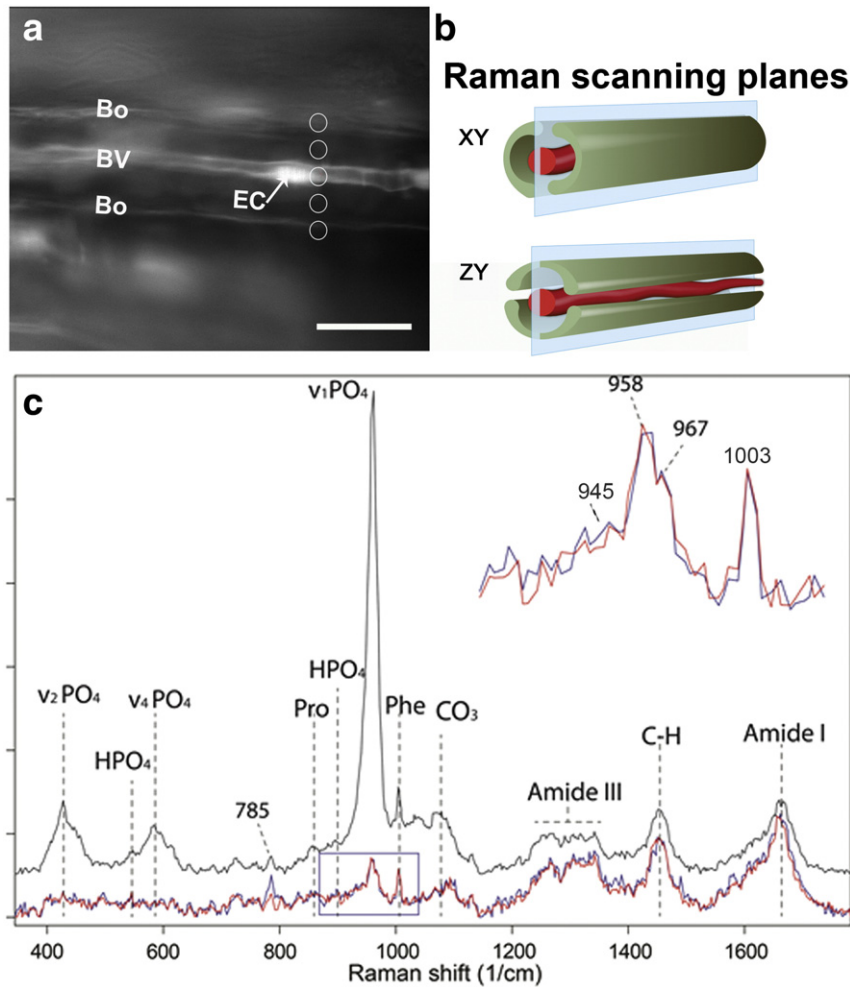
**Fig. 5.** In vivo fluorescence-Raman imaging (a) Confocal image taken in the XY plane, of one hemi-cylinder bone with a blood vessel located at the center. Calcein labels the bones (Bo) and EGFP the ECs and blood vessel (BV). The EC carries a homogeneous fluorescence signal in the cytoplasm of the cell, resulting in the fluorescence marker of the blood vessel wall. The high fluorescence signal in the center of the EC is contributed to the nucleus region of the EC. The micrograph was taken in vivo using the correlative fluorescence-Raman microscopy. The white circles correspond to the Raman laser beam size. Scale bar 20 μm. (b) Schematic figures of the planes scanned using the correlative fluorescence-Raman microscopy. (c) Raman spectrum of bone (black) and two spectra of mineral aggregates located between two hemi-cylinders of one ray (red and blue). Inset: enlargement of the region delineated by the rectangle.

mechanisms for ion transport involve direct and fast pathways involving cells from endothelial cell lineage. During this time, the forming bone is relatively thin (1–2 μm) and less compact compared to adult zebrafish fin bone (~10 μm) [12]. When the initial skeleton is complete, the bones start thickening and increasing in overall size. We presume that the bone lining cells and osteoblasts are actively involved in this stage of bone formation, whereas in the larval stage they may be less active.

One type of mineral deposit that we identified is located relatively far from the mineralizing bone, but is in close proximity to blood vessels. Some of these mineral particles have sizes of several microns and do contain calcium and phosphorous. We have not identified their mineral phase, nor do we know that this mineral is ultimately deposited in the bone. Their presence at some distance from the forming bone raises the possibility that this mineral may have additional functions. We do however note that within a short time after their deposition, the distal ends of the forming bones will be close to this region, raising the possibility that these are reservoirs of mineral to be used for future bone mineralization.

A different group of mineral deposits is found in intracellular locations, between bone rays and in close proximity to the forming bone. Surprisingly, the cells containing the mineral deposits were identified as belonging to the endothelial cells lineage based on the expression of DsRed driven by the *fli1* promoter. This implies that at least some of the cells that line the forming bone outer surface are endothelial in origin. The possibility that osteoblasts differentiate from endothelial cells was proposed in studies that describe the intimate relationship between the capillary system and bone in different animal models such as sheep and mouse [56–58]. It was suggested that endothelial cells and/or pericytes could serve as precursors for osteoblasts, and hence take an active part in bone formation. Furthermore, recent studies reported on coupling of angiogenesis and osteogenesis by a specific vessel subtype in bone [59].

The (pre)osteoblasts observed in the *Tg(osx:mCherry)* fish, were located mainly at the edges of the forming bone hemi-cylinders, and only rarely next to their flat surfaces. The location of the pre-osteoblasts at the edges of the hemi-cylinders coincides with that of the $fli1^+$ cells. Taken together, this indicates that at this stage of larval development, bone mineralization occurs mostly at the edges of the hemi-cylinder surfaces. The $osx^+$ cells that are located at the center of the hemi-cylinder and line the bone surface, are more elongated than the $osx^+$ cells at the edges, and resemble mature osteoblasts as characterized by TEM in human and rat bones [60,61]. Cryo-SEM shows intracellular cluster of vesicles in the same locations where mature osteoblasts are observed (Fig. 4c,d), and calcein-labeled particles are observed by in vivo imaging at similar locations.

Mahamid et al. observed mineral vesicles in cells located next to the bones in the adult zebrafish tail, using cryo-SEM [12]. However, the cells were not shown to be osteoblasts. Knopf and coworkers [26] followed the formation of new bones in the mature zebrafish tail after amputation using three different osteoblast markers (*runx2*, *osterix* and *osteocalcin*), and observed osteoblasts located along the direction of growth of the bone rays. No information is available, however, on whether these osteoblasts were associated with mineral deposits. The data reported here are in agreement with the observations by Mahamid et al. and Knopf et al. [12,26], and provide a more comprehensive view of mineral deposition and cell activity during the initial stages of bone formation in *larval* zebrafish.

The mineral phase was investigated using in vivo Raman microspectroscopy coupled with fluorescence imaging, which provided spatially resolved chemical information. The spectral features observed in locations corresponding to intra-cellular mineral deposits (main $PO_4$ peak positions: 955–958, 967, 945 $cm^{-1}$), suggest that the mineral phase in the aggregates is similar to the phase that was observed by Crane et al. in the coronal sutures of embryonic mice tissue culture. Crane et al. [17] identified a complex mixture of amorphous calcium phosphate and disordered OCP-like mineral phases. No evidence for a polyphosphate phase (reported in murine bone forming cells (16)), which is expected to have peaks at 700 and 1180 $cm^{-1}$ [[62], was observed. The mineral aggregates that we observed between bone hemi-cylinders are presumably intra-cellular, and represent the earliest stage of mineralization. As such, we do not expect them to be a crystalline phase, but rather a disordered calcium phosphate phase complex, which may have some characteristics of an octacalcium phosphate mineral.

The Raman spectra also reveal the presence of nucleic acid-like molecules in close proximity to the mineral. Due to the limited axial resolution, we were not able to determine whether these nucleic acid-like molecules are directly associated with the mineral phase or if they appear in the spectra as a result of averaging the signal of the mineral aggregate with that coming from the surrounding tissue. We note that ATP has been reported to be associated directly with ACP in the crab hepatopancreas [63] and that in vitro studies showed that ATP delays the conversion of ACP to crystalline carbonated apatite [64]. The presence of DNA-like species in association with the mineral phases introduces an interesting perspective on the possible role of such species in stabilizing transient disordered phases on their way to the mineralized tissue.

## 5. Conclusions

We demonstrate the presence of mineral aggregates in close proximity to the blood vessels, between and within the intra-ray region, and relatively far from the bone. The aggregates consist of a disordered calcium phosphate phase with characteristic features of OCP. The observation that mineral particles form at diverse locations, and involve different cell types including cells which express *fli1* fluorescent reporter entails a conceptual change in our understanding of the comprehensive mechanism of bone formation in vertebrates, from the blood to the bone.

Supplementary data to this article can be found online at http://dx.doi.org/10.1016/j.bone.2015.02.020.

## References

[1] Fleming WR. Calcium metabolism of teleosts. Am Zool 1967;7(4):835–42.
[2] Kuyper AC. The chemistry of bone formation: II. Some factors which affect the solubility of calcium phosphate in blood serum. J Biol Chem 1945;159(2):417–24.
[3] Mody N, Tintut Y, Radcliff K, Demer LL. Vascular calcification and its relation to bone calcification: possible underlying mechanisms. J Nucl Cardiol 2003;10(2):177–83.
[4] Jahnen-Dechent W, Schafer C, Ketteler M, McKee MD. Mineral chaperones: a role for fetuin-A and osteopontin in the inhibition and regression of pathologic calcification. J Mol Med 2008;86(4):379–89.
[5] O'Young J, et al. Matrix Gla protein inhibits ectopic calcification by a direct interaction with hydroxyapatite crystals. J Am Chem Soc 2011;133(45):18406–12.
[6] Luo G, et al. Spontaneous calcification of arteries and cartilage in mice lacking matrix GLA protein. Nature 1997;386(6620):78–81.
[7] Holt C, Sorensen ES, Clegg RA. Role of calcium phosphate nanoclusters in the control of calcification. FEBS J 2009;276(8):2308–23.
[8] Heiss A, et al. Structural basis of calcification Inhibition by α2-HS glycoprotein/fetuin-A: formation of colloidal calciprotein particles. J Biol Chem 2003;278(15):13333–41.
[9] Boonrungsiman S, et al. The role of intracellular calcium phosphate in osteoblast-mediated bone apatite formation. Proc Natl Acad Sci U S A 2012;109(35):14170–5.
[10] Golub EE. Role of matrix vesicles in biomineralization. Biochim Biophys Acta 2009;12(8):26.
[11] Mahamid J, et al. Bone mineralization proceeds through intracellular calcium phosphate loaded vesicles: a cryo-electron microscopy study. J Struct Biol 2011;174(3):527–35.
[12] Mahamid J, et al. Mapping amorphous calcium phosphate transformation into crystalline mineral from the cell to the bone in zebrafish fin rays. Proc Natl Acad Sci U S A 2010;107(14):6316–21.
[13] Gay C, Schraer H. Frozen thin-sections of rapidly forming bone: bone cell ultrastructure. Calcif Tissue Res 1975;19(1):39–49.
[14] Schraer H, Gay CV. Matrix vesicles in newly synthesizing bone observed after ultracryotomy and ultramicroincineration. Calcif Tissue Res 1977;23(2):185–8.
[15] Wu LN, et al. Physicochemical characterization of the nucleational core of matrix vesicles. J Biol Chem 1997;272(7):4404–11.
[16] Omelon S, et al. Control of vertebrate skeletal mineralization by polyphosphates. PLoS One 2009;4(5):0005634.
[17] Crane NJ, Popescu V, Morris MD, Steenhuis P, Ignelzi Jr MA. Raman spectroscopic evidence for octacalcium phosphate and other transient mineral species deposited during intramembranous mineralization. Bone 2006;39(3):434–42.
[18] Brown WE. Octacalcium phosphate and hydroxyapatite: crystal structure of octacalcium phosphate. Nature 1962;196(4859):1048–50.
[19] Cheng P-T. Octacalcium phosphate formation in vitro: implications for bone formation. Calcif Tissue Int 1985;37(1):91–4.
[20] Füredi-Milhofer H, Purgarić B, Brečević L, Pavković N. Precipitation of calcium phosphates from electrolyte solutions. Calcif Tissue Res 1971;8(1):142–53.
[21] Iijima M, et al. Precipitation of octacalcium phosphate at 37 °C and at pH 7.4: in relation to enamel formation. J Cryst Growth 1991;112(2):467–73.
[22] Kobayashi K, et al. Osteoconductive property of a mechanical mixture of octacalcium phosphate and amorphous calcium phosphate. ACS Appl Mater Interfaces 2014;6(24):22602–11.
[23] Lawson ND, Weinstein BM. In vivo imaging of embryonic vascular development using transgenic zebrafish. Dev Biol 2002;248(2):307–18.
[24] Hogan BM, et al. Ccbe1 is required for embryonic lymphangiogenesis and venous sprouting. Nat Genet 2009;41(4):396–8.
[25] Flores MV, et al. Duplicate zebrafish runx2 orthologues are expressed in developing skeletal elements. Gene Expr Patterns 2004;4(5):573–81.
[26] Knopf F, et al. Bone regenerates via dedifferentiation of osteoblasts in the zebrafish fin. Dev Cell 2011;20(5):713–24.
[27] Li N, Felber K, Elks P, Croucher P, Roehl HH. Tracking gene expression during zebrafish osteoblast differentiation. Dev Dyn 2009;238(2):459–66.

[28] Sousa S, et al. Differentiated skeletal cells contribute to blastema formation during zebrafish fin regeneration. Development 2011;138(18):3897–905.

[29] Singh SP, Holdway JE, Poss KD. Regeneration of amputated zebrafish fin rays from de novo osteoblasts. Dev Cell 2012;22(4):879–86.

[30] Spoorendonk KM, Hammond CL, Huitema LFA, Vanoevelen J, Schulte-Merker S. Zebrafish as a unique model system in bone research: the power of genetics and in vivo imaging. J Appl Ichthyol 2010;26(2):219–24.

[31] Fisher S, Franz-Odendaal T. Evolution of the bone gene regulatory network. Curr Opin Genet Dev 2012;22(4):390–7.

[32] Kessels MY, et al. Proteomics analysis of the zebrafish skeletal extracellular matrix. PLoS One 2014;9(3):e90568.

[33] Landis WJ, Geraudie J. Organization and development of the mineral phase during early ontogenesis of the bony fin rays of the trout *Oncorhynchus mykiss*. Anat Rec 1990;228(4):383–91.

[34] Tu S, Johnson Stephen L. Fate restriction in the growing and regenerating zebrafish fin. Dev Cell 2011;20(5):725–32.

[35] Huang CC, et al. Collagen IX is required for the integrity of collagen II fibrils and the regulation of vascular plexus formation in zebrafish caudal fins. Dev Biol 2009; 332(2):360–70.

[36] Du SJ, Frenkel V, Kindschi G, Zohar Y. Visualizing normal and defective bone development in zebrafish embryos using the fluorescent chromophore calcein. Dev Biol 2001;238(2):239–46.

[37] Parichy DM, Elizondo MR, Mills MG, Gordon TN, Engeszer RE. Normal table of postembryonic zebrafish development: staging by externally visible anatomy of the living fish. Dev Dyn 2009;238(12):2975–3015.

[38] Wallach DFH, Surgenor DM, Soderberg J, Delano E. Preparation and properties of 3,6-dihydroxy-2,4-bis-[N-N′-di-(carboxymethyl)-aminomethyl] fluoran. Anal Chem 1959;31(3):456–60.

[39] Moran AL. Calcein as a marker in experimental studies newly-hatched gastropods. Mar Biol 2000;137(5–6):893–8.

[40] Avraham-Davidi I, et al. ApoB-containing lipoproteins regulate angiogenesis by modulating expression of VEGF receptor 1. Nat Med 2012;18(6):967–73.

[41] Lister JA, Robertson CP, Lepage T, Johnson SL, Raible DW. Nacre encodes a zebrafish microphthalmia-related protein that regulates neural-crest-derived pigment cell fate. Development 1999;126(17):3757–67.

[42] Vatine GD, et al. Zebrafish as a model for monocarboxyl transporter 8-deficiency. J Biol Chem 2013;288(1):169–80.

[43] Spoorendonk KM, et al. Retinoic acid and Cyp26b1 are critical regulators of osteogenesis in the axial skeleton. Development 2008;135(22):3765–74.

[44] Ben Shoham A, et al. S1P1 inhibits sprouting angiogenesis during vascular development. Development 2012;139(20):3859–69.

[45] Bennet M, et al. Simultaneous fluorescence-Raman imaging of bone mineralization in living zebrafish larvae. Biophys J 2014;106(4):L17–9.

[46] Sauer GR, Zunic WB, Durig JR, Wuthier RE. Fourier transform Raman spectroscopy of synthetic and biological calcium phosphates. Calcif Tissue Int 1994;54(5):414–20.

[47] Kazanci M, Fratzl P, Klaushofer K, Paschalis EP. Complementary information on in vitro conversion of amorphous (precursor) calcium phosphate to hydroxyapatite from Raman microspectroscopy and wide-angle X-ray scattering. Calcif Tissue Int 2006;79(5):354–9.

[48] Fowler BO, Markovic M, Brown WE. Octacalcium phosphate.3. Infrared and Raman vibrational-spectra. Chem Mater 1993;5(10):1417–23.

[49] Short KW, Carpenter S, Freyer JP, Mourant JR. Raman spectroscopy detects biochemical changes due to proliferation in mammalian cell cultures. Biophys J 2005;88(6):4274–88.

[50] Matthaus C, Boydston-White S, Miljkovic M, Romeo M, Diem M. Raman and infrared microspectral imaging of mitotic cells. Appl Spectrosc 2006;60(1):1–8.

[51] Stone N, Kendall C, Smith J, Crow P, Barr H. Raman spectroscopy for identification of epithelial cancers. Faraday Discuss 2004;126:141–57.

[52] Ruiz-Chica J, Medina MA, Sanchez-Jimenez F, Ramirez FJ. Fourier transform Raman study of the structural specificities on the interaction between DNA and biogenic polyamines. Biophys J 2001;80(1):443–54.

[53] Vidavsky N, et al. Initial stages of calcium uptake and mineral deposition in sea urchin embryos. Proc Natl Acad Sci U S A 2014;111(1):39–44.

[54] Le Gros Clark WE. The tissues of the body, an introduction to the study of anatomy. Acad Med 1958;33(9):xviii–xxii.

[55] Olsen BR, Reginato AM, Wang W. Bone development. Annu Rev Cell Dev Biol 2000; 16:191–220.

[56] Decker B, Bartels H, Decker S. Relationships between endothelial cells, pericytes, and osteoblasts during bone formation in the sheep femur following implantation of tricalciumphosphate-ceramic. Anat Rec 1995;242(3):310–20.

[57] Maes C, et al. Osteoblast precursors, but not mature osteoblasts, move into developing and fractured bones along with invading blood vessels. Dev Cell 2010;19(2): 329–44.

[58] Medici D, et al. Conversion of vascular endothelial cells into multipotent stem-like cells. Nat Med 2010;16(12):1400–6.

[59] Kusumbe AP, Ramasamy SK, Adams RH. Coupling of angiogenesis and osteogenesis by a specific vessel subtype in bone. Nature 2014;507(7492):323–8.

[60] Marks Jr SC, Popoff SN. Bone cell biology: the regulation of development, structure, and function in the skeleton. Am J Anat 1988;183(1):1–44.

[61] Miller S, Jee WS. The bone lining cell: a distinct phenotype? Calcif Tissue Int 1987; 41(1):1–5.

[62] Majed N, Matthäus C, Diem M, Gu AZ. Evaluation of intracellular polyphosphate dynamics in enhanced biological phosphorus removal process using Raman microscopy. Environ Sci Technol 2009;43(14):5436–42.

[63] Becker GL, Chen CH, Greenawalt JW, Lehninger AL. Calcium phosphate granules in the hepatopancreas of the blue crab *Callinectes sapidus*. J Cell Biol 1974;61(2): 316–26.

[64] Posner AS, Betts F, Blumenthal NC. Properties of nucleating systems. Metab Bone Dis Relat Res 1978;1(2):179–83.